

Quiet Submillimeter MR Imaging of the Lung Is Feasible with a PETRA Sequence at 1.5 T¹

Gaël Dournes, MD, PhD
 David Grodzki, PhD
 Julie Macey, MD
 Pierre-Olivier Girodet, MD, PhD
 Michaël Fayon, MD, PhD
 Jean-François Chateil, MD, PhD
 Michel Montaudon, MD, PhD
 Patrick Berger, MD, PhD
 François Laurent, MD

Purpose:

To assess lung magnetic resonance (MR) imaging with a respiratory-gated pointwise encoding time reduction with radial acquisition (PETRA) sequence at 1.5 T and compare it with imaging with a standard volumetric interpolated breath-hold examination (VIBE) sequence, with extra focus on the visibility of bronchi and the signal intensity of lung parenchyma.

Materials and Methods:

The study was approved by the local ethics committee, and all subjects gave written informed consent. Twelve healthy volunteers were imaged with PETRA and VIBE sequences. Image quality was evaluated by using visual scoring, numbering of visible bronchi, and quantitative measurement of the apparent contrast-to-noise ratio (CNR) and signal-to-noise ratio (SNR). For preliminary clinical assessment, three young patients with cystic fibrosis underwent both MR imaging and computed tomography (CT). Comparisons were made by using the Wilcoxon signed-rank test for means and the McNemar test for ratios. Agreement between CT and MR imaging disease scores was assessed by using the κ test.

Results:

PETRA imaging was performed with a voxel size of 0.86 mm³. Overall image quality was good, with little motion artifact. Bronchi were visible consistently up to the fourth generation and in some cases up to the sixth generation. Mean CNR and SNR with PETRA were 32.4% \pm 7.6 (standard deviation) and 322.2% \pm 37.9, respectively, higher than those with VIBE ($P < .001$). Good agreement was found between CT and PETRA cystic fibrosis scores ($\kappa = 1.0$).

Conclusion:

PETRA enables silent, free-breathing, isotropic, and submillimeter imaging of the bronchi and lung parenchyma with high CNR and SNR and may be an alternative to CT for patients with cystic fibrosis.

© RSNA, 2015

Online supplemental material is available for this article.

¹From the Center for Cardiothoracic Research of Bordeaux, University of Bordeaux, Bordeaux, France (G.D., P.O.G., M.F., M.M., P.B., F.L.); Inserm, Center for Cardiothoracic Research of Bordeaux, U1045, F-33000, 146 rue Léo Saignat, 33076 Bordeaux, France (G.D., P.O.G., M.F., M.M., P.B., F.L.); Department of Thoracic and Cardiovascular Imaging, Department of Respiratory Disease, Department of Functional and Respiratory Examination, Centre Hospitalier Universitaire (CHU) de Bordeaux, Pessac, France (G.D., J.M., P.O.G., M.M., P.B., F.L.); Department for Imaging of the Woman and Child, Pediatric Pneumology Unit, CHU de Bordeaux, Bordeaux, France (M.F., J.F.C.); CHU de Bordeaux, CIC 0005, Bordeaux, France (M.F.); and Department of Magnetic Resonance, Siemens Healthcare, Erlangen, Germany (D.G.). Received August 14, 2014; revision requested October 1; revision received November 3; accepted November 16; final version accepted December 23. **Address correspondence to F.L.** (e-mail: gael.dournes@chu-bordeaux.fr).

Computed tomography (CT) is the modality of choice for lung imaging because of its high spatial resolution and good contrast between air and lung tissue. Conversely, lung magnetic resonance (MR) imaging suffers from inherent technical difficulties, such as very low proton density, cardiac and chest motion, and the decaying of transverse relaxation time due to susceptibility effects. However, lung MR imaging is a nonionizing technique, and recent reports (1–3) about the risk of developing cancers with cumulated x-ray exposures indicate that radiation-free alternatives to CT are required. Therefore, there is a need for robust lung MR imaging sequences that would allow advantages comparable to those of CT, such as submillimeter spatial resolution, sufficient lung parenchyma signal, no need for contrast material injection, and isotropic voxel dimensions for three-dimensional multiplanar reconstruction. A short echo time has been shown to be crucial in improving the quality of lung proton MR images (4). The pointwise encoding time reduction with radial acquisition (PETRA) sequence is a noiseless prototype hybrid approach to ultrashort-echo time three-dimensional imaging (5,6) that has been shown to achieve the shortest possible encoding time for a given imaging unit (7) without the need for a hardware change. Although conventional pulse sequences are efficient for depicting clinically relevant information in chronic lung diseases (8–13), there are well-known shortcomings in

imaging bronchi up to the lobar level and imaging lung signal (14). We hypothesized that the use of the PETRA sequence would help correct these known inaccuracies. Thus, we aimed to assess lung imaging with a respiratory-gated PETRA sequence at 1.5 T in comparison with a standard volumetric interpolated breath-hold examination (VIBE) sequence (15), with extra focus on the visibility of the bronchi and lung parenchyma signal.

Materials and Methods

Siemens Healthcare (Erlangen, Germany) provided technical support. One author (D.G.) is employed by Siemens Healthcare. All authors who are not employees of Siemens Healthcare had full control over the data at all stages of the project.

Subjects

The study was approved by the local ethics committee, and all subjects gave written informed consent. Twelve healthy volunteers (four women [mean age, 29.6 years \pm 1.1 {standard deviation}] and eight men [mean age, 28.0 years \pm 2.4]; $P = .39$) with a mean weight of 61.2 kg \pm 3.4 were examined. They had no history of smoking, no clinical manifestation of respiratory disorders, and no history of lung disease. Informed consent was obtained after a full explanation of the MR imaging procedure. Qualitative and quantitative assessment of all anonymized image data sets was performed independently in random order and then in final consensus by two experienced readers (G.D. [observer 1] and F.L. [observer 2], with 10 and 30 years of experience in chest imaging, respectively).

MR Imaging Protocols and PETRA Sequence

MR imaging was performed with a 1.5-T MR imaging unit (Magnetom Avanto;

Siemens Healthcare). A 12-phased-array body coil was used for detection. Patients were positioned in the supine position with arms raised above the body. Parameters of the PETRA sequence were as follows: repetition time msec/echo time msec, 4.1/0.07; field of view, 360 mm³; and matrix size, 416 mm³. Details of the unenhanced PETRA and VIBE protocols are provided in Table E1 (online). The PETRA sequence is an ultrashort-echo time sequence that has been previously reported (7) in which the imaging gradients are already switched on during a hard low-flip-angle nonselective excitation (Fig 1). After the excitation, the acquisition of radial half-projections is begun as early as allowed by the hardware at time $t =$ echo time after the middle of the excitation pulse. Because encoding of spins already effectively starts at the middle of the pulse, points in the center of k-space are missed during the switching time from transmission to receive mode. These points are acquired single-point-wise on a Cartesian grid. In the current implementation, data with isotropic dimensions are collected. To take lung motion into account, an adaptive respiratory gating method involving a respiratory bellows signal was used. In

Advances in Knowledge

- The noiseless pointwise encoding time reduction with radial acquisition (PETRA) sequence enables high-spatial-resolution three-dimensional lung MR imaging with a submillimeter voxel size of 0.86 mm³.
- The PETRA sequence enables lung MR imaging with high contrast-to-noise (32.4% \pm 7.6 [standard deviation]) and signal-to-noise (322.2% \pm 37.9) ratios without the need for contrast material enhancement.

Implication for Patient Care

- PETRA MR imaging represents a noiseless, radiation-free alternative to CT in imaging the bronchi and lung parenchyma with submillimeter resolution.

Published online before print

10.1148/radiol.15141655 Content codes: **CH** **MR**

Radiology 2015; 276:258–265

Abbreviations:

CNR = contrast-to-noise ratio

PETRA = pointwise encoding time reduction with radial acquisition

ROI = region of interest

SNR = signal-to-noise ratio

VIBE = volumetric interpolated breath-hold examination

Author contributions:

Guarantors of integrity of entire study, G.D., P.O.G., M.F., P.B., F.L.; study concepts/study design or data acquisition or data analysis/interpretation, all authors; manuscript drafting or manuscript revision for important intellectual content, all authors; manuscript final version approval, all authors; agrees to ensure any questions related to the work are appropriately resolved, all authors; literature research, G.D., D.G., P.B., F.L.; clinical studies, G.D., J.M., P.O.G., M.F., J.F.C., P.B.; experimental studies, G.D., D.G., J.M., P.B.; statistical analysis, G.D., M.M., P.B.; and manuscript editing, G.D., D.G., P.O.G., J.F.C., M.M., P.B., F.L.

Conflicts of interest are listed at the end of this article.

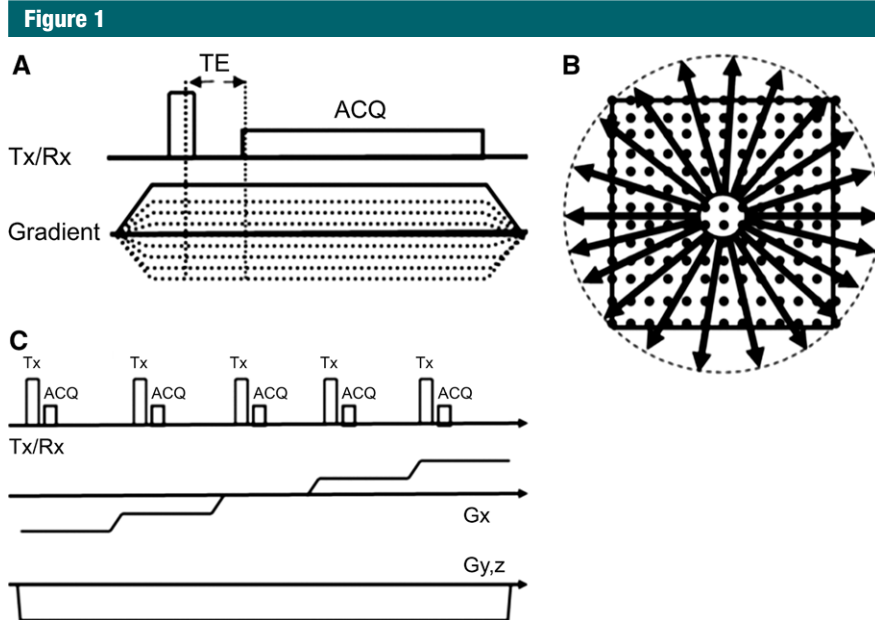


Figure 1: Chart of PETRA sequence. *B*, After the gradient ramp-up, a hard low-flip-angle pulse is applied, and readout is started at time $t = \text{echo time (TE)}$. *B*, As encoding starts at $t = 0$, k-space points in the center of k-space are missed. *C*, The gap is completely filled with exact measured Cartesian k-space points by using single-point imaging. *ACQ* = acquisition, *G_x* = gradient along x-axis, *G_{y,z}* = gradient along y-axis and z-axis, *Rx* = k-space point readout, *Tx* = encoding time after excitation.

this study, we used a 30% threshold to accept end-expiratory data and reject inspiratory data. For image reconstruction, the k-space has to be filled up on a Cartesian grid. Points acquired in the Cartesian part are simply gridded to their corresponding positions, whereas data for the radial part have to be weighted with a density matrix (16,17). This density matrix was adapted to the density of points in the Cartesian center of k-space with methods that have been previously described (18).

Semiquantitative Assessment of Image Quality

The visibility of fissures was graded according to the following scale: A grade of 0 indicated that fissures were not present on the image; a grade of 1, that the image was uninterpretable; a grade of 2, fair visibility; a grade of 3, good partial visibility; and a grade of 4, good complete visibility. The level of visible airways and vessels was rated by using the following system: A rating of 0 indicated the lobar level; a rating of 1, the segmental level; a rating of 2, the subsegmental

level; a rating of 3, superior to the subsegmental level; and a rating of 4, up to the distal lung periphery. Lung signal homogeneity was graded as follows: A grade of 0 indicated no signal; a grade of 1, poor homogeneity; a grade of 2, fair homogeneity; a grade of 3, good homogeneity; and a grade of 4, very good homogeneity. Motion artifacts were rated by using the following system: A rating of 0 indicated that no lung structure was recognizable; a rating of 1, important artifact; a rating of 2, moderate artifact; a rating of 3, slight artifact; and a rating of 4, no artifact.

Quantitative Assessment of Visible Bronchi

Numbering of the visible bronchi was performed by using the Boyden classification system, with generation three corresponding to the segmental level (19).

Quantitative Assessment of Lung Signal Intensity

Regions of interest (ROIs) of the same shape (circle) and size (56 mm²) were

manually placed by two independent observers (G.D. and F.L.) in the axial plane by using Myrian software (Intrasense, Montpellier, France). ROIs corresponding to signal intensity (SI) within air were placed in the trachea and in the right and left main bronchus, and data in these ROIs were averaged to calculate SI_{airway} . ROIs corresponding to SI within vessels were traced in the pulmonary trunk and in the right and left main pulmonary arteries, and data in these ROIs were averaged to calculate SI_{vessel} . Three axial sections were selected for the assessment of SI in the lung parenchyma: one at the level of the crossing of the aorta, one at the level of the carina, and one at the level of the pulmonary inferior veins. ROIs were placed at each location in the anterior part and posterior part of the right and left lung, respectively, at least 2 cm from the lung periphery. Vessels were carefully avoided when ROIs were traced. Data in the 12 resulting ROIs were averaged to calculate SI_{lung} . The mean value between readers was used for analysis. Apparent contrast-to-noise ratio (CNR) and apparent signal-to-noise ratio (SNR) were calculated as follows (20,21): $CNR = (SI_{\text{lung}} - SI_{\text{airway}}) / SI_{\text{vessel}} \cdot 100\%$ and $SNR = (SI_{\text{lung}} / SI_{\text{airway}}) \cdot 100\%$.

Clinical Application in Cystic Fibrosis

For future clinical application, we present our preliminary experience in three young adults, including two young men (mean age, 21.5 years \pm 0.7) and one 20-year-old young woman, with cystic fibrosis. They were referred to our institution for routine follow-up, including CT. Patient 1 was a 21-year-old man whose body mass index (BMI) was 23 and whose predicted forced expiratory volume in 1 second (FEV₁) was 94%. He had no chronic bronchial infection. Patient 2 was a 20-year-old woman, with a BMI of 19 and an FEV₁ of 50% predicted. She had chronic bronchial infection with *Staphylococcus aureus*. Patient 3 was a 22-year-old man with a BMI of 17 and an FEV₁ of 35% predicted. He had chronic bronchial infection with *Pseudomonas aeruginosa*. All

three patients were homozygous for the $\Delta F508$ mutation. Informed consent was obtained to perform additional lung MR imaging with the unenhanced PETRA and VIBE protocols (Table E1 [online]). Quantification of disease severity at imaging was performed by using the scoring system of Bhalla et al (22).

Statistical Analysis

Results are expressed as means \pm standard deviations for continuous variables and as absolute numbers for categorical variables. Comparison of means was performed by using the Wilcoxon signed-rank test (23), and comparison of categorical variables was performed by using the McNemar test (24). Interobserver reproducibility was assessed with Bland-Altman analysis (25). Agreement between CT and MR imaging was assessed by using the κ test (24). $P < .05$ was considered to indicate a significant difference.

Results

Semiquantitative Assessment of Image Quality

Results of visual scoring are given in Table 1 and are illustrated in Figure 2. Statistically significant differences were found regarding the visibility of fine structures such as lung fissures, bronchi, and small vessels ($P < .001$). There was no difference in lung signal homogeneity ($P = .055$). Although respiratory gating was used, motion artifacts were still more pronounced on PETRA images because of residual motions of the lung bases ($P < .001$). However, these artifacts did not impair mean overall image quality (20.0 ± 1.2 for PETRA and 13.5 ± 1.6 for VIBE; $P < .001$).

Quantitative Assessment of Visible Bronchi per Generation

Table 2 shows that there was complete visualization of bronchi up to the subsegmental level with PETRA, whereas bronchi were visually missing starting from the segmental level with VIBE ($P < .001$). Bronchi remained visible up to the sixth bronchial generation with PETRA (Fig 3).

Table 1

Lung MR Image Quality Scores with PETRA and VIBE Sequences in 12 Healthy Volunteers

Image Quality Parameter	PETRA (n = 12)	VIBE (n = 12)	P Value*
Visibility of fissures	3.8 \pm 0.4	0.3 \pm 0.5	<.001
Visibility of bronchi	2.8 \pm 0.4	1.2 \pm 0.8	<.001
Visibility of vessels	4.0 \pm 0.0	2.4 \pm 0.5	<.001
Signal homogeneity	3.0 \pm 0.4	3.5 \pm 0.5	.055
Motion artifact			
Cardiac	3.1 \pm 0.4	2.4 \pm 0.5	<.001
Respiratory	2.8 \pm 0.4	3.7 \pm 0.5	<.001
Overall summed score	20.0 \pm 1.2	13.5 \pm 1.6	<.001

Note.—Data are means \pm standard deviations.

* Calculated with the Wilcoxon signed-rank test.

Figure 2

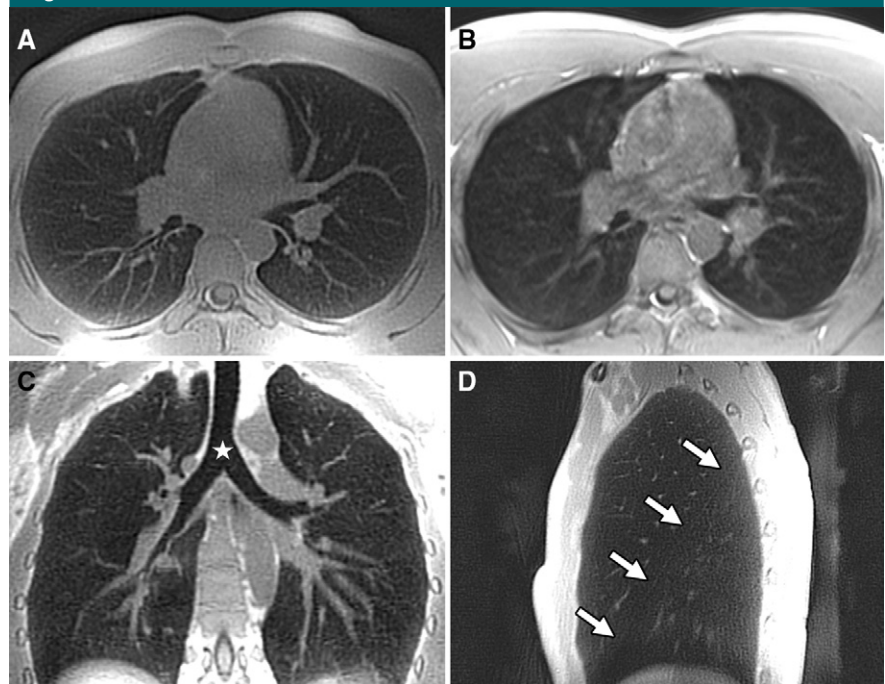


Figure 2: A, B, Axial PETRA (repetition time msec/echo time msec, 4.1/0.07; flip angle, 6°) and VIBE (3.3/1.18; flip angle, 8°) lung MR images in 28-year-old male volunteer. A, Image obtained with PETRA sequence shows conspicuous visibility of bronchi and vessels to the distal lung periphery, as compared with, B, image obtained with VIBE sequence. On, C, a coronal multiplanar reconstruction, \star = air in the trachea, clearly different in signal intensity from the adjacent lung parenchyma. On, D, a sagittal reconstruction, arrows = complete visibility of the left fissure.

Quantitative Assessment of Lung Parenchymal Signal

An example of ROI placement is given in Figure E1 (online). The mean difference of the measurements was -3.2 (95% confidence interval [CI]:

$-45.0, 38.6$) with PETRA and 0.2 (95% CI: $-9.6, 10.2$) with VIBE (Fig E2 [online]). Details on the regional assessment of CNR and SNR with PETRA are given in Table E2 (online). Table 2 indicates that the mean CNR

was $32.4\% \pm 7.6$ and the mean SNR was $322.2\% \pm 37.9$ for PETRA, with both values being considerably higher than those with the VIBE sequence ($P < .001$ for both).

Initial Experience in Cystic Fibrosis

Figure 4 shows axial images in patient 1. CT and PETRA images (Fig 4, A and B) show subtle changes in wall thickening and lumen dilatation starting from the posterior segmental bronchus of the right upper lobe and visible up to the eighth generation. Figure 5 shows coronal reconstructions in patient 2. A similar change in parenchymal attenuation and signal intensity between CT (Fig 5, A) and unenhanced PETRA MR imaging (Fig 5, B) was observed.

Table 2

Quantitative Assessment of Bronchi and Lung Parenchyma Signal Intensity with PETRA and VIBE in 12 Healthy Volunteers

Parameter	PETRA (n = 12)	VIBE (n = 12)	PValue
No. of visible bronchi*			
Generation 0	12/12	12/12	> .99
Generation 1	24/24	24/24	> .99
Generation 2	60/60	60/60	> .99
Generation 3	240/240	153/240	< .001
Generation 4	480/480	82/480	< .001
Generation 5	185/960	0/960	< .001
Generation 6	42/1920	0/1920	< .001
Generation 7	0/3840	0/3840	> .99
Lung parenchyma signal intensity†			
CNR (%)	32.4 ± 7.6	1.6 ± 1.9	< .001
SNR (%)	322.2 ± 37.9	120.0 ± 31.8	< .001

* Data are absolute numbers of visible bronchi/theoretical number of bronchi expected at each generation.

† Data are means \pm standard deviations.

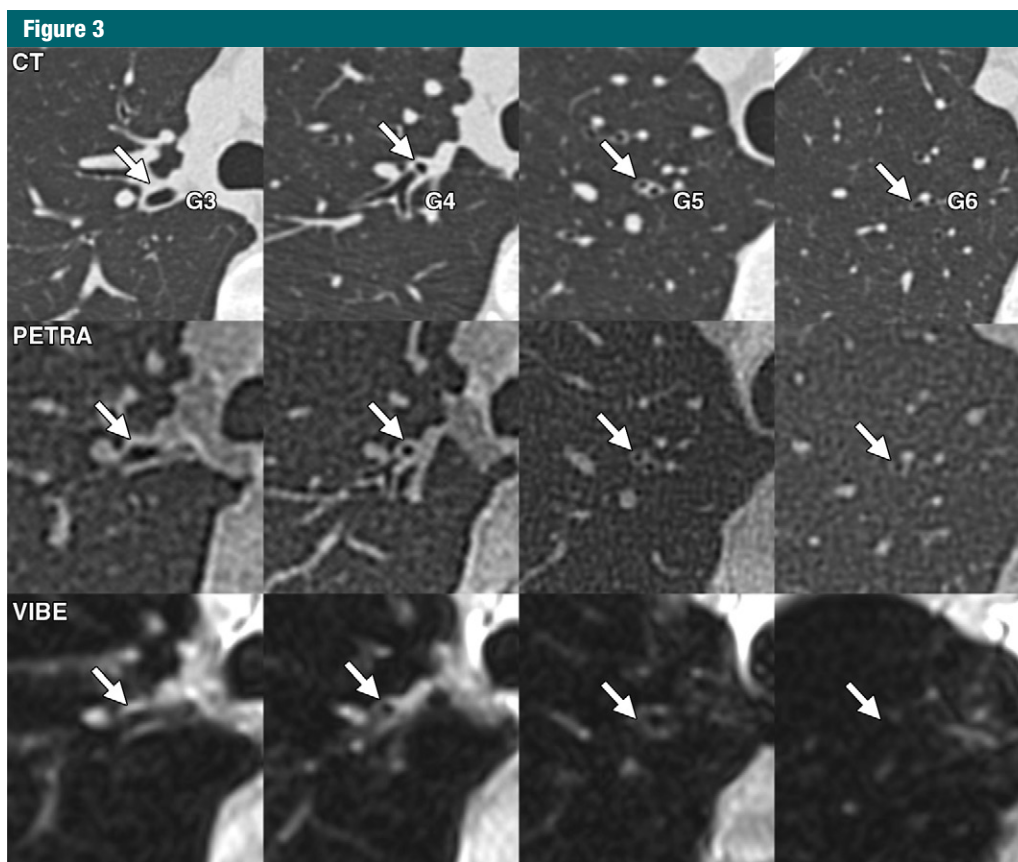


Figure 3: Axial CT and MR images show example of bronchial path starting from the segmental right upper lobe bronchus in a 33-year-old healthy male volunteer who underwent CT 3 months after an episode of posttraumatic pneumothorax. MR imaging was performed the same day. Arrows = bronchi at each generation. Bronchi from the third generation (G3) to the sixth generation (G6) are visible on both CT images (upper row) and PETRA MR images (4.1/0.07; flip angle, 6°) (middle row). On unenhanced VIBE MR images (3.3/1.18; flip angle, 8°) (lower row), bronchi are visible from the third to the fourth (G4) generation.

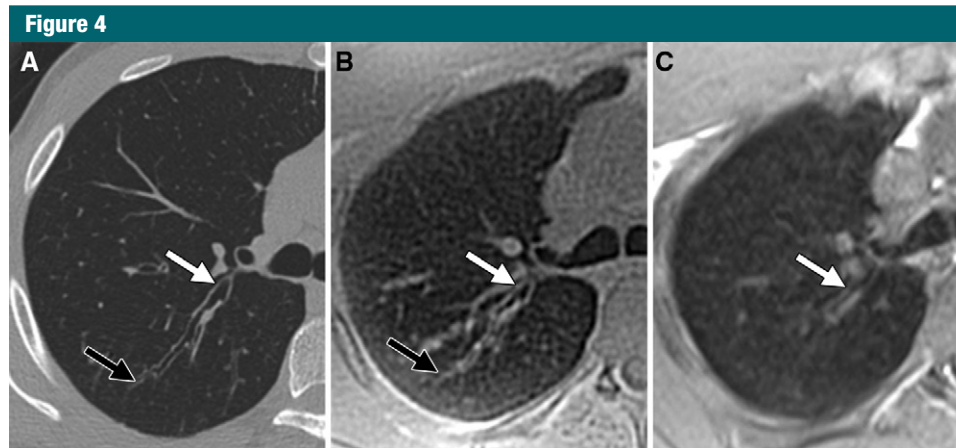


Figure 4: Axial, *A*, CT and, *B*, *C*, MR images of the lung acquired with, *B*, PETRA (4.1/0.07; flip angle, 6°) and, *C*, VIBE (3.3/1.18; flip angle, 8°) in a 21-year-old man with cystic fibrosis. There is moderate bronchiectasis from the third (white arrows) to the eighth (black arrows) generations of the posterior segmental bronchus of right upper lobe that is visible with both, *A*, CT and, *B*, the PETRA sequence. With, *C*, the VIBE sequence, bronchial paths are visible up to the third (segmental) generation only. The Bhalla score was 5 at both CT and PETRA imaging.

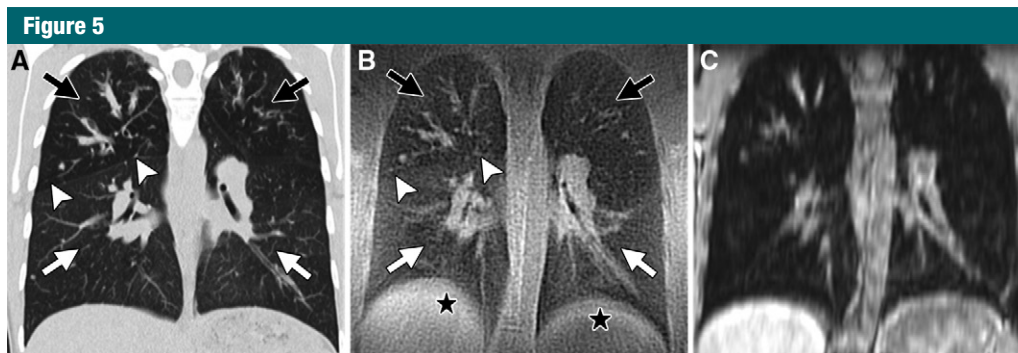


Figure 5: Coronal, *A*, CT, *B*, PETRA (4.1/0.07; flip angle, 6°), and, *C*, VIBE (3.3/1.18; flip angle, 8°) images in 20-year-old woman with cystic fibrosis. The Bhalla score was 10 at both CT and PETRA imaging. Black arrows = areas of decreased lung attenuation on, *A*, concordant with decreased signal intensity on, *B*, visible in the lung apices. White arrows = normal signal from the lung bases. Arrowheads indicate the major right lung fissure, clearly delineating these two areas at both CT and PETRA imaging. ★ = Residual motion artifact at the level of the diaphragm.

Figure 6 shows images in patient 3. Owing to severe dyspnea and cough, this patient could not hold his breath. With the use of free-breathing PETRA, the CT and MR images appear to show close agreement. In all three patients, Bhalla scores at CT and unenhanced MR imaging showed 100% agreement ($\kappa = 1.0$), despite the fact that motion artifacts were visible in the MR imaging studies of patients 2 and 3.

Discussion

Our study demonstrates the feasibility of a noiseless, free-breathing,

three-dimensional, isotropic MR imaging sequence with submillimeter spatial resolution (0.86 mm³) in imaging the bronchi and lung parenchyma with substantial SNR and CNR at 1.5 T.

PETRA offers several advantages for lung MR imaging. The gradient is already switched on during k-space encoding; therefore, there is no gradient delay and no eddy current (7). Hence there is no shading or streaking artifact related to disturbed trajectories. In addition, PETRA allows the shortest encoding time for a given imaging unit without the need for hardware change (7) and thus allows the detection of

substantial signal from short T2 species. In the present study, an additional respiratory gating method was introduced, and results showed that submillimeter lung MR imaging was feasible with little motion artifact in healthy volunteers. Moreover, PETRA is almost noiseless because of its unique gradient-pulse characteristics, without sacrificing SNR or CNR (5). Therefore, the long acquisition time associated with respiratory synchronization was not a problem because the volunteers and patients did not experience noise discomfort. This is a nonnegligible characteristic for future application

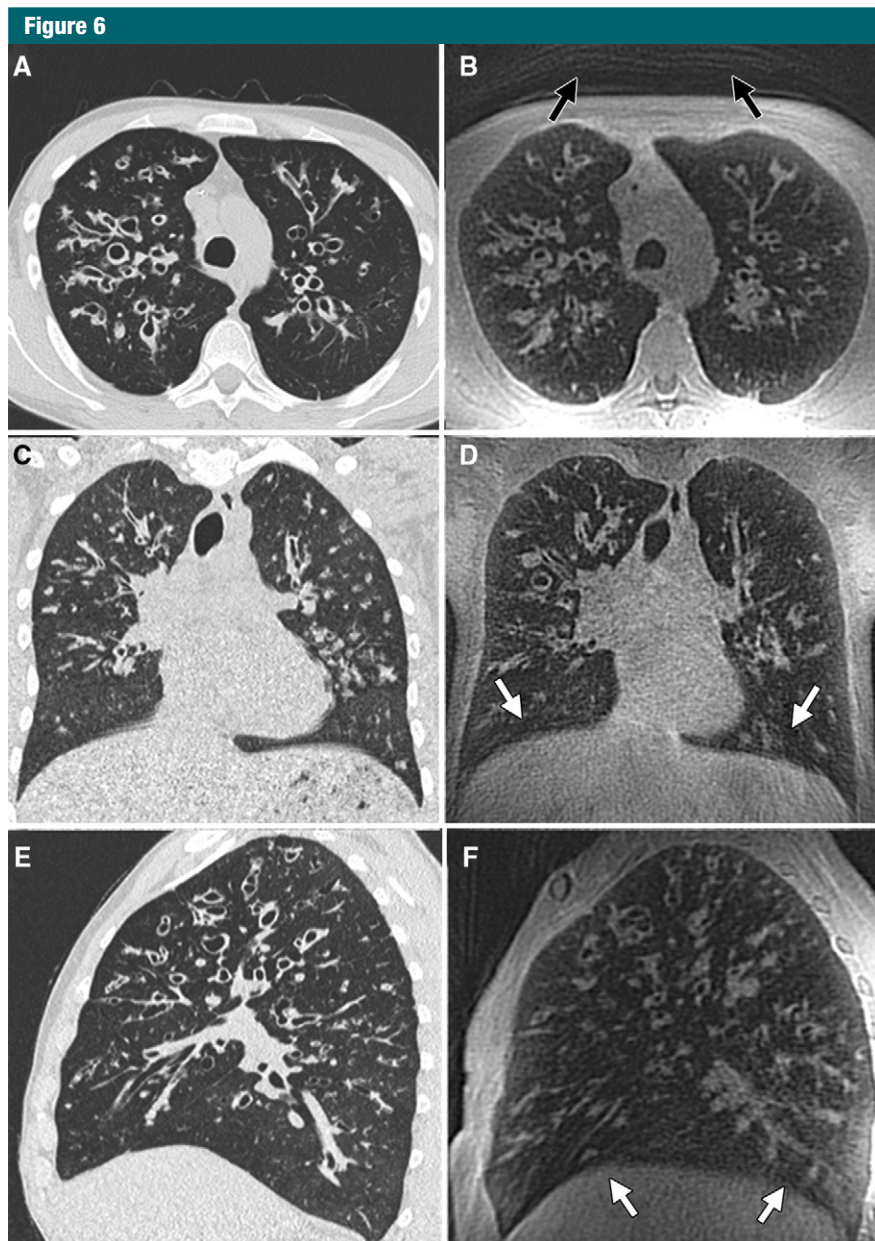


Figure 6: A, C, E, CT and, B, D, F, PETRA (4.1/0.07; flip angle, 6°) images in a 22-year-old man with severe cystic fibrosis. Images were reconstructed in the, A, B, axial, C, D, coronal, and, E, F, sagittal planes. Breath-holding maneuvers were impossible for the patient to perform because of severe dyspnea and cough. The voxel size at CT was 0.7 mm³, and the voxel size at PETRA imaging was 0.86 mm³. On, B, arrows = structural artifact related to motion during MR image acquisition and represent the chest wall at different levels of inflation. On, D and F, arrows = blurring of the lung bases caused by motion artifacts. However, clinical interpretation was not impaired, and the Bhalla scores were 13 at both CT and PETRA imaging, with 100% agreement for all parameters.

in children. Indeed, infants are prone to be afraid of MR imaging. They are also often afraid of needles; some of them are simply not willing to undergo

contrast material-enhanced MR imaging. We have not yet experienced the effect of contrast material injection on lung signal intensity. The use of PETRA

appeared to provide a change in parenchymal signal similar to that seen on CT images without contrast enhancement.

This study had some limitations. We compared the PETRA sequence with the VIBE sequence only. However, as reviewed by Altes et al (14), the shortcomings of bronchi and lung signal visibility with conventional sequences are well known, and we specifically aimed at evaluating the ability of PETRA to solve these established drawbacks. A comparison between PETRA and another standard ultrashort-echo time sequence was not available with the same machine. For instance, a hard pulse is needed with the PETRA sequence, whereas different pulses can be applied with the ultrashort-echo time sequence (20), with no limit in flip angle or shape. However, potential issues in hard pulse section selectivity have been previously investigated, and a correction involving sinc-shaped frequency excitation has been found to work (26). In addition, PETRA is a three-dimensional imaging technique only, whereas two-dimensional and three-dimensional imaging are possible with the ultrashort-echo time sequence. Moreover, there was no oversampling, and volunteers and patients had to raise arms to prevent aliasing (20). Finally, there were respiratory motion artifacts with PETRA, whereas VIBE was excellent at not generating them. Nevertheless, we aimed to demonstrate the performance of PETRA in disease conditions, when breathing patterns are irregular and unpredictable episodes of cough occur. Clinical interpretation was not altered in these conditions. Last, VIBE is a robust T1-weighted sequence that has been reported to be clinically useful in various chronic respiratory diseases, including cystic fibrosis (8–10), emphysema (11), sarcoidosis (12), pneumonia (13), and lung nodules (27).

In conclusion, on the basis of our results, future MR imaging evaluation, including qualitative and/or quantitative evaluation of PETRA images, may be an attractive field of investigation for radiation-free imaging of the lung with high spatial resolution.

Acknowledgments: The study was achieved within the context of Laboratory of Excellence TRAIL, ANR-10-LABX-57.

Disclosures of Conflicts of Interest: **G.D.** disclosed no relevant relationships. **D.G.** Activities related to the present article: none to disclose. Activities not related to the present article: is an employee of Siemens Healthcare. Other relationships: none to disclose. **J.M.** disclosed no relevant relationships. **P.O.G.** Activities related to the present article: none to disclose. Activities not related to the present article: has received fees for lectures from Novartis, Pierre Fabre, and Almirall; has received travel fees from Novartis and Chiesi. Other relationships: none to disclose. **M.F.** disclosed no relevant relationships. **J.F.C.** disclosed no relevant relationships. **M.M.** disclosed no relevant relationships. **P.B.** Activities related to the present article: none to disclose. Activities not related to the present article: is a member of the boards of Novartis, GSK, and Boehringer Ingelheim; has received research grants from GSK and Pierre Fabre; has received fees for lectures from Novartis, GSK, Takeda, Chiesi, and Astra-Zeneca; has received travel fees from Novartis, GSK, Takeda, Chiesi, Boehringer Ingelheim, and Astra-Zeneca. Other relationships: has submitted U.S. patent no. 12/487,273 regarding bronchial smooth muscle remodeling involving calcium-dependent enhanced mitochondrial biogenesis in asthma. **F.L.** disclosed no relevant relationships.

References

- Brenner DJ, Hall EJ. Cancer risks from CT scans: now we have data, what next? *Radiology* 2012;265(2):330–331.
- Puderbach M, Eichinger M. The role of advanced imaging techniques in cystic fibrosis follow-up: is there a place for MRI? *Pediatr Radiol* 2010;40(6):844–849.
- Pearce MS, Salotti JA, Little MP, et al. Radiation exposure from CT scans in childhood and subsequent risk of leukaemia and brain tumours: a retrospective cohort study. *Lancet* 2012;380(9840):499–505.
- Ohno Y, Nishio M, Koyama H, et al. Pulmonary 3 T MRI with ultrashort TEs: influence of ultrashort echo time interval on pulmonary functional and clinical stage assessments of smokers. *J Magn Reson Imaging* 2014;39(4):988–997.
- Ida M, Wakayama T, Nielsen ML, Abe T, Grodzki DM. Quiet T1-weighted imaging using PETRA: initial clinical evaluation in intracranial tumor patients. *J Magn Reson Imaging* 2014;41(2):447–453.
- Heismann B, Ott M, Grodzki D. Sequence-based acoustic noise reduction of clinical MRI scans. *Magn Reson Med* 2014 May 29. [Epub ahead of print]
- Grodzki DM, Jakob PM, Heismann B. Ultra-short echo time imaging using pointwise encoding time reduction with radial acquisition (PETRA). *Magn Reson Med* 2012;67(2):510–518.
- Wielpütz MO, Puderbach M, Kopp-Schneider A, et al. Magnetic resonance imaging detects changes in structure and perfusion, and response to therapy in early cystic fibrosis lung disease. *Am J Respir Crit Care Med* 2014;189(8):956–965.
- Eichinger M, Heussel CP, Kauczor HU, Tidens H, Puderbach M. Computed tomography and magnetic resonance imaging in cystic fibrosis lung disease. *J Magn Reson Imaging* 2010;32(6):1370–1378.
- Sileo C, Corvol H, Boelle PY, Blondiaux E, Clement A, Ducou Le Pointe H. HRCT and MRI of the lung in children with cystic fibrosis: comparison of different scoring systems. *J Cyst Fibros* 2014;13(2):198–204.
- Ley-Zaporozhan J, Ley S, Eberhardt R, Kauczor HU, Heussel CP. Visualization of morphological parenchymal changes in emphysema: comparison of different MRI sequences to 3D-HRCT. *Eur J Radiol* 2010;73(1):43–49.
- Chung JH, Little BP, Forssen AV, et al. Proton MRI in the evaluation of pulmonary sarcoidosis: comparison to chest CT. *Eur J Radiol* 2013;82(12):2378–2385.
- Attenberger UI, Morelli JN, Henzler T, et al. 3 Tesla proton MRI for the diagnosis of pneumonia/lung infiltrates in neutropenic patients with acute myeloid leukemia: initial results in comparison to HRCT. *Eur J Radiol* 2014;83(1):e61–e66.
- Altes TA, Eichinger M, Puderbach M. Magnetic resonance imaging of the lung in cystic fibrosis. *Proc Am Thorac Soc* 2007;4(4):321–327.
- Biederer J, Both M, Graessner J, et al. Lung morphology: fast MR imaging assessment with a volumetric interpolated breath-hold technique: initial experience with patients. *Radiology* 2003;226(1):242–249.
- Pipe JG, Menon P. Sampling density compensation in MRI: rationale and an iterative numerical solution. *Magn Reson Med* 1999;41(1):179–186.
- Jackson JI, Meyer CH, Nishimura DG, Macovski A. Selection of a convolution function for Fourier inversion using gridding [computerised tomography application]. *IEEE Trans Med Imaging* 1991;10(3):473–478.
- Pipe JG. Reconstructing MR images from undersampled data: data-weighting considerations. *Magn Reson Med* 2000;43(6):867–875.
- Boyden EA. Lateral views of the segmental bronchi and related pulmonary vessels in an injected preparation of the lungs. *Radiology* 1953;61(2):183–188.
- Johnson KM, Fain SB, Schiebler ML, Nagle S. Optimized 3D ultrashort echo time pulmonary MRI. *Magn Reson Med* 2013;70(5):1241–1250.
- Ma W, Sheikh K, Svenningsen S, et al. Ultra-short echo-time pulmonary MRI: evaluation and reproducibility in COPD subjects with and without bronchiectasis. *J Magn Reson Imaging* 2014 Jun 26. [Epub ahead of print]
- Bhalla M, Turcios N, Aponte V, et al. Cystic fibrosis: scoring system with thin-section CT. *Radiology* 1991;179(3):783–788.
- Wilcoxon F. Individual comparisons of grouped data by ranking methods. *J Econ Entomol* 1946;39(2):269.
- Langenbucher J, Labouvie E, Morgenstern J. Measuring diagnostic agreement. *J Consult Clin Psychol* 1996;64(6):1285–1289.
- Bland JM, Altman DG. Statistical methods for assessing agreement between two methods of clinical measurement. *Lancet* 1986;1(8476):307–310.
- Grodzki DM, Jakob PM, Heismann B. Correcting slice selectivity in hard pulse sequences. *J Magn Reson* 2012;214(1):61–67.
- Chandarana H, Heacock L, Rakheja R, et al. Pulmonary nodules in patients with primary malignancy: comparison of hybrid PET/MR and PET/CT imaging. *Radiology* 2013;268(3):874–881.

dergone changes since the time of our retrospective data review. Furthermore, unfortunately, there is no single universally accepted surgical approach for the treatment of endometrial carcinoma, and the practice remains non-uniform between Europe and North America, as well as amongst different institutions within North America.

Second, as Dr Thomassin-Naggara and colleagues accurately note, 50% of patients in our cohort had LVSI, which is higher than that in other reports. This may be explained by the fact that we selected patients with tumors that were large enough to undergo quantitative assessment with MR volumetry.

Third, we could not directly correlate tumor volumes at MR imaging to those at histopathologic examination because this information was not consistently available at the time of our retrospective data review.

Fourth, we would like to direct Dr Thomassin-Naggara and colleagues to table 5 and to the “Qualitative Assessment of Myometrial Invasion” section under Results for further information regarding the comparison of T2-weighted imaging with diffusion-weighted imaging and T2-weighted imaging with contrast-enhanced T1-weighted imaging in the assessment of myometrial invasion. We did not perform a subgroup analysis to examine the influence of various confounding factors such as menopausal status and benign uterine abnormalities on the performance of MR imaging for the assessment of myometrial invasion because this analysis was previously reported by Beddy et al (2).

Finally, in this study we aimed to investigate the value of quantitative tumor volume measurements and whole tumor volume apparent diffusion coefficient histogram metrics as predictive biomarkers of the depth of myometrial invasion, tumor grade, and LVSI at surgery. Although beyond the scope of our study, we concur with Dr Thomassin-Naggara and colleagues that it would be of interest for future studies to in-

vestigate how quantitative MR imaging criteria could influence surgical management of endometrial carcinoma in accordance with ESMO practice guidelines (3).

Disclosures of Conflicts of Interest: S.N. disclosed no relevant relationships. C.R. disclosed no relevant relationships. Y.L. disclosed no relevant relationships. B.G. disclosed no relevant relationships. E.S. disclosed no relevant relationships.

References

1. Nougaret S, Reinhold C, Alsharif SS, et al. Endometrial cancer: combined MR volumetry and diffusion-weighted imaging for assessment of myometrial and lymphovascular invasion and tumor grade. *Radiology* 2015;276(3):797-808.
2. Beddy P, Moyle P, Kataoka M, et al. Evaluation of depth of myometrial invasion and overall staging in endometrial cancer: comparison of diffusion-weighted and dynamic contrast-enhanced MR imaging. *Radiology* 2012;262(2):530-537.
3. Colombo N, Preti E, Landoni F, et al. Endometrial cancer: ESMO clinical practice guidelines for diagnosis, treatment and follow-up. *Ann Oncol Off J Eur Soc Med Oncol ESMO* 2013;24(Suppl 6):vi33-vi38.

Errata

Originally published in:

Radiology 2014;273(1):175-184
DOI:10.1148/radiol.14132593

The Alzheimer Structural Connectome: Changes in Cortical Network Topology with Increased Amyloid Plaque Burden

Jeffrey W. Prescott, Arnaud Guidon, P. Murali Doraiswamy, Kingshuk Roy Choudhury, Chunlei Liu, Jeffrey R. Petrella; For the Alzheimer's Disease Neuroimaging Initiative

Erratum in:

Radiology 2016;279(1):328
DOI:10.1148/radiol.2016164007

Correspondence should be listed as follows: Address correspondence to **J.R.P. (e-mail: jeffrey.petrella@duke.edu)**. This has been updated online.

Originally published in:

Radiology 2015;276(1):258-265
DOI: 10.1148/radiol.15141655

Quiet Submillimeter MR Imaging of the Lung Is Feasible with a PETRA Sequence at 1.5 T

Gaël Dournes, David Grodzki, Julie Macey, Pierre-Olivier Girodet, Michaël Fayon, Jean-François Chateil, Michel Montaudon, Patrick Berger, François Laurent

Erratum in:

Radiology 2016;279(1):328
DOI:10.1148/radiol.2016164006

The following Acknowledgment should be listed: **This study was achieved within the context of Laboratory of Excellence TRAIL, ANR-10-LABX-57**. This has been updated online.

Originally published in:

Radiology 2016;278(2):316-332
DOI: 10.1148/radiol.2015150364

Beyond the Cuff: MR Imaging of Labroligamentous Injuries in the Athletic Shoulder

Elizabeth A. Roy, Ian Cheyne, Gordon T. Andrews, Bruce B. Forster

Erratum in:

Radiology 2016;279(1):328
DOI:10.1148/radiol.2016164008

Incorrect Learning Objectives were published with the print article. The Learning Objectives should be as follows: **Describe correct MR imaging technique for assessment of labroligamentous injuries of the shoulder; Define common labral variants that can simulate injury; Discuss examples of sequelae of traumatic instability; Describe the SLAP tear and its major components; Discuss the concepts of external and internal impingement and their major subcategories; Describe the common nerve entrapment syndromes and their major imaging characteristics.**